Reactive and Functional Polymers 196 (2024) 105833

Contents lists available at ScienceDirect

Reactive and Functional Polymers

journal homepage: www.elsevier.com/locate/react

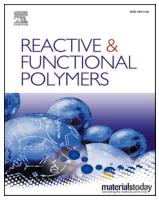

Dielectric characterisation of chitosan-based composite membranes containing fractionated kraft and organosolv lignin

M.H. Wolf [a], N. Izaguirre [b], B. Pascual-José [a], R. Teruel-Juanes [a], J. Labidi [b], A. Ribes-Greus [a,*]

[a] Materials Technological Institute (ITM), Universitat Politècnica de València (UPV), Camino de Vera, s/n, 46022 Valencia, Spain
[b] Chemical and Environmental Engineering Department, Faculty of Engineering of Gipuzkoa, Universidad del País Vasco (UPV/EHU), Plaza Europa 1, 20018 Donostia-San Sebastián, Spain

ARTICLE INFO

Keywords:
Dielectric thermal analysis (DETA)
Biobased materials
Chitosan
Lignin
Solvent fractionation

ABSTRACT

Chitosan-based composite membranes with fractionated kraft and organosolv lignin were prepared by solvent casting. A small lignin fraction (1%) was added to the neat chitosan to obtain a good distribution. The influence of lignin extraction with ethyl acetate and consequently ethanol on the dielectric and conductive properties of the composites was investigated by dielectric thermal analysis (DETA). Overall, the chitosan-lignin composites exhibit three relaxation mechanisms (β, β_{wet}, and α) and two conductivity phenomena (σ and MWS). FTIR analysis showed that the composites with organosolv lignin fractions have fewer hydroxyl groups than those with kraft lignin, which decreases slightly further for both after ethanol extraction. The lignin fractions with lower molecular weight and higher OH content show stronger interactions with chitosan, due to hydrogen bonding. These interactions affect the thermal activation and cooperativity of the β-, β_{wet}, and α-relaxation. Furthermore, the kraft lignin fractions with many polar groups are very compatible with the chitosan matrix, resulting in a more compact structure and higher fragility. The membranes CS OL_{EA} and CS KL_E have a lower electron conductivity and a higher proton conductivity. Thus, they have promising conductivity properties for fuel cell applications.

1. Introduction

Limited reserves, rising prices, and the destructive environmental impact of petrochemical resources are promoting the research of bio-based materials. Cellulose, lignin, chitin, and starch among others, which can be derived from industrial waste products, represent potential alternatives, due to their great availability, low cost, and high biodegradability [1].

Chitin, which is found in crustacean shells, insect cuticles, green algae and cell walls of fungi and yeasts can be extracted from the residual waste of the seafood processing industry [2]. Chitosan, deacetylated chitin, possesses abundant amino groups, that allow easier processing with improved solubility, due to potential protonation in acidic media and also tailoring of properties through chemical functionalisation [3].

Lignin, one of the main components of wood along with cellulose and hemicellulose can be obtained as a by-product from the paper industry in different processes [4]: (i) from kraft pulping, the most widely used pulping process [5], and (ii) from pulp by organic solvent treatment, which is usually less contaminated, highly phenolic, and of low molecular weight [6]. Lignin is well suited as a filler material for chitosan in wastewater treatment systems [7,8], tissue engineering [9], energy conversion [10,11], encapsulation [12,13], and as wood adhesives [14].

Nevertheless, lignin's complex chemical structure and vastly heterogeneous properties, depending on its origin and the preparation method, limit its wide utilisation in composite materials [15]. Solvent fractionation is a process that uses solvents of varying polarity to separate lignin into different fractions that can purify its properties and remove contaminants, such as carbohydrates, proteins, and inorganic materials [16]. In particular, the fractionation of lignin has shown to effectively modify the molecular weight, functional groups, antioxidant activity, thermal stability and sorption properties [17,18]. Izaguirre et al. prepared chitosan composite films by incorporating different percentages of lignin fractions to improve the UV absorbance and modify their mechanical properties [19]. Nonetheless, still little is known about the relationship between the characteristics of lignin fractions and the performance of lignin-based composites.

Dielectric thermal analysis (DETA) is a useful technique to provide

* Corresponding author.
E-mail address: aribes@ter.upv.es (A. Ribes-Greus).

https://doi.org/10.1016/j.reactfunctpolym.2024.105833
Received 31 July 2023; Received in revised form 15 December 2023; Accepted 9 January 2024
Available online 11 January 2024

information on the molecular structure as well as the electron and proton conductivity of membranes [20]. The dielectric spectra of pure chitosan has been comprehensively discussed in the literature [21–26] and the effect of fillers on the dielectric properties of chitosan composites have been shown [27–30]. However, the interactions between different lignin fractions and the polymer matrix are not very well known and their understanding allows to explore the potential use and extend the application range of such biocomposites.

The aim of this work is to study the dielectric and conductive properties of chitosan-based membranes when distinct types of fractionated lignin (kraft and organosolv) are added. Fourier-transform infrared spectroscopy (FTIR) allows the analysis of differences in composition and functional groups of the composites caused by the addition of lignin fractions after extraction in a first step with ethyl acetate and subsequently in the second step with ethanol. These structural differences alter the dielectric spectrum and impact the thermal activation and cooperativity of the relaxations. In the same way, the electron and proton conductivity can be modified due their relationship to the molecular structure and conductive phenomena. The properties of the chitosan-lignin composites may suggest a new use of these membranes as electrolytes in fuel cell applications.

2. Experimental

2.1. Materials

Pulping kraft liquor of eucalyptus was kindly provided by the paper mill Papelera Guipuzcoana de Zikuñaga, S.A. (Hernani, Spain). The liquor had a pH of 12.6 and a lignin content of ~44 g·L^{-1}. Organosolv lignin (CAS: 8068-03-9) was purchased from Chemical Point (Oberhaching, Germany). Microcrystalline chitosan powder with a molecular weight (M_w) of 500.000 g·mol^{-1} and a degree of deacetylation of 98% were purchased from Mahtani Chitosan Pvt. Ltd. (Veraval, India). Ethyl acetate (≥99.5%) provided from Fisher Scientific UK (Loughborough, United Kingdom) and ethanol (absolute) supplied from Scharlab (Barcelona, Spain) were used for the sequential organic solvent fractionation. Acetic acid (technical) for solubilizing chitosan and sulfuric acid (96%) for lignin precipitation was purchased from PanReac Química SLU (Barcelona, Spain).

2.2. Lignin preparation and fractionation

The preparation of the kraft lignin (*KL*) and organosolv lignin (*OL*) is described in detail by Izaguirre et al. [19]. KL was precipitated from black liquor with sulfuric acid, filtered through a 0.22 μm nylon filter and washed with distilled water. OL was used as provided. Fig. 1 demonstrates the employed lignin fractionation process based on the method by Tagami et al. [17].

In summary, ethyl acetate (*EA*) and ethanol (*E*) were sequentially used to fractionate both *KL* and *OL*, according to the capacity of each solvent to individually dissolve lignin. 50 g of lignin were dissolved in 1 L of organic solvent for 2 h at room temperature under stirring. The soluble fraction was separated from the insoluble fraction and recovered by evaporation and precipitation. The insoluble fraction was dried at 50 °C. A thorough characterisation of the kraft lignin, organosolv lignin, and their individual fractions was carried out by Izaguirre et al. [19].

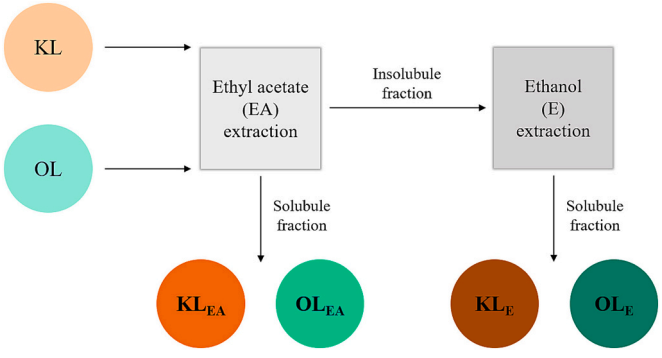

Fig. 1. Subsequential solvent fractionation process of kraft lignin (KL) and organosolv lignin (OL) with ethyl acetate (EA) and ethanol (E).

2.3. Preparation of biocomposite membranes by solvent casting method

The preparation of the chitosan-lignin composite membranes by solvent casting is described by Izaguirre et al. [19]. Chitosan was dissolved in 1% (*v*/v) aqueous acetic acid at room temperature under stirring. The lignin fractions were dissolved in acetone (c = 0.5 g/L) and then added to the chitosan solution with a concentration of 1% ($w_{Lignin}/w_{Chitosan}$). Following, the solutions were homogenised with a T25 ULTRA-TURRAX® disperser from IKA, filtered, degassed, and poured (20 mL) in petri dishes with a diameter of 90 mm. Lastly the mixtures were placed in a Unimax 1010 incubator from Heidolph at 30 °C overnight for the solvent to evaporate. Fig. 2 shows the prepared chitosan-lignin composite membranes and the proposed structure composites with their main functional groups and possible interactions. The water uptake of the biocomposites has been determined by thermogravimetric analysis: CS KL_{EA} = 13.3%, CS KL_E = 10.8%, CS OL_{EA} = 12.2%, CS OL_E = 12.7%.

2.4. Physico-chemical characterisation

2.4.1. Fourier-transform infrared spectroscopy (FTIR)

FTIR analysis was performed using a Nicolet iS50 FTIR Spectrometer from Thermo Scientific (Waltham, USA) with the iS50 ATR accessory. The spectra were collected in the range from 4000 to 500 cm^{-1} with at a resolution of 4 cm^{-1} and 32 scans. Backgrounds spectra were collected before each sequence of experiments. For each material 5 spectra at different positions were collected and the average spectra was calculated and used for further discussion. The spectra of the composite membranes were normalised at the band for the ring stretching of the polysaccharide structures at 895 cm^{-1} for proper comparison.

2.4.2. Dielectric thermal analysis (DETA)

DETA analysis was carried out using a Broadband Dielectric Impedance Spectrometer from Novocontrol Technologies GmbH & Co. KG (Montabaur, Germany) with an Alpha-A Frequency Response Analyser. A BDS-1200 Novocontrol parallel-plated capacitor with two plated electrodes was used as dielectric test cell. The sample electrode assembly consisted of two stainless-steel electrodes (20 mm diameter) filled with the sample. The measurement of the dielectric spectra was conducted in the frequency range 10^{-2} to 10^{7} Hz under isothermal conditions by increasing steps of 10 °C between −150 and 180 °C. For the measurement of the proton conductivity of the composites, the samples were previously placed in deionised water for 1 h at 30 °C and then measured through-plane in the frequency range of 10^{0} to 10^{7} Hz between 20 and 80 °C by increasing isothermal steps of 5 °C. All the measurements were carried out in an inert nitrogen (N_2) atmosphere.

2.5. Theory section

The dielectric response of polymers can be described in terms of the real part (ε') and the imaginary part (ε") of the complex permittivity (ε*) and with the material's loss factor (tan δ). The spectra of the imaginary permittivity (ε") were deconvoluted using the Charlesworth method [31] by adding all the necessary equations of Havriliak–Negami (HN) functions (Eq. (1)) [32,33].

$$\varepsilon' - \varepsilon_\infty = \sum Im\left[\frac{\Delta\varepsilon}{\{1+(i\omega\tau_{HN})^{\alpha_{HN}}\}^{\beta_{HN}}}\right] \quad (1)$$

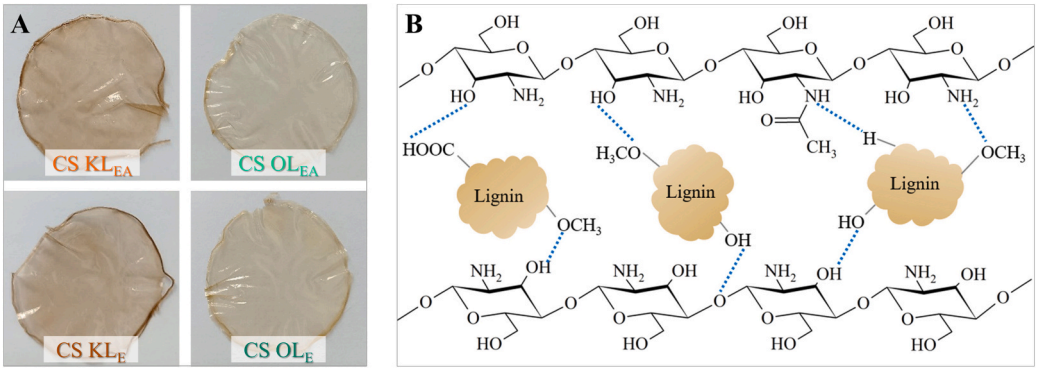

Fig. 2. (A) Chitosan composite membranes after solvent casting containing different lignin fractions; CS KL_{EA}, CS KL_{E}, CS OL_{EA}, and CS OL_{E}. (B) Proposed chemical structure and interactions of the chitosan-lignin composites.

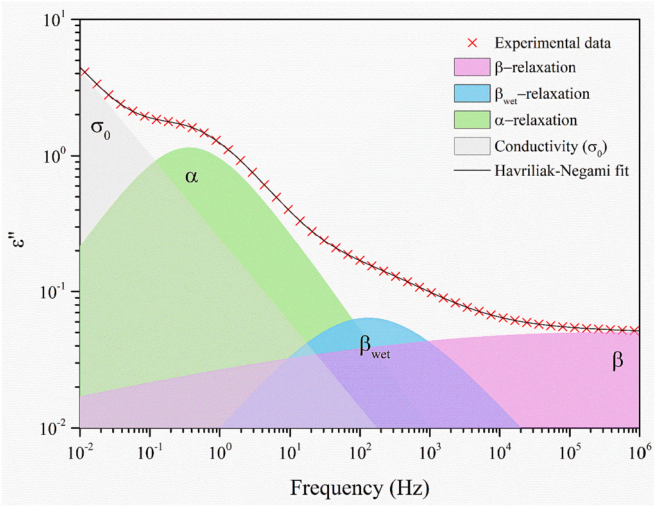

Fig. 3. Havriliak-Negami fit of the imaginary permittivity (ε") of CS KL_{EA} at 0 °C. The deconvolution includes the β-relaxation, β_{wet}-relaxation, α-relaxation, and a conductivity contribution (σ_0).

where ε_∞ is the real permittivity at high frequencies, $\Delta\varepsilon$ is the dielectric strength, τ_{HN} is the Havriliak-Negami relaxation time, ω is the angular frequency and α_{HN} and β_{HN} are parameters corresponding to the width and asymmetry broadening of the relaxation peak. Fig. 3 represents an exemplary Havriliak-Negami fit to the experimental data consisting of three distinctive relaxation processes and a conductivity contribution at lower frequencies.

The relaxation time τ_{max}, representing the most probable relaxation time of the molecular process, is obtained from the relaxation time and the shape parameters from the HN deconvoluted curves at each temperature according to Eq. (2) [34].

$$\tau_{max} = \tau_{HN}\left[\frac{sin\left(\frac{\pi(\alpha_{HN})\beta_{HN}}{2(\beta_{HN}+1)}\right)}{sin\left(\frac{\pi(\alpha_{HN})}{2(\beta_{HN}+1)}\right)}\right]^{\frac{1}{\alpha_{HN}}} \quad (2)$$

The temperature dependency of the relaxation times contains important information about the thermal activation of the relaxation mechanisms. The relaxations showing a linear temperature dependency can be explained by means of the Arrhenius function [35], and the relaxations with a non-linear temperature dependency can be described with the Vogel–Fulcher–Tammann–Hesse (VFTH) function [35], according to Eqs. (3) and (4), respectively.

$$f_{max} = f_0 \cdot e^{\left(\frac{-E_a}{R \cdot T}\right)} \quad (3)$$

where f_{max} is the maximum frequency, being $f_{max} = 1/(2\cdot\pi\cdot\tau_{max})$; f_0 is a pre-exponential term, E_a the activation energy, and R is the universal gas constant ($R = 8.314\ J\cdot K^{-1}\cdot mol^{-1}$).

$$f_{max} = f_0 \cdot e^{\left(\frac{-D\cdot T_V}{T-T_V}\right)} \quad (4)$$

where T_V is the Vogel temperature, below which polymer segments become immobile, and D is the fragility parameter that determines the variation from an Arrhenius behaviour.

Various parameters describing different aspects of the materials can be derived from the VFTH fit, such as the fragility index m, the free volume coefficient Φ_g, the thermal expansion coefficient α_g, and the apparent activation energy related to the glass transition temperature Ea_{Tg} were calculated according to Eqs. (5) to (8), respectively [36,37].

$$m = \frac{\partial\, log(\tau)}{\partial\left(\frac{T_g}{T}\right)^{T=T_g}} = \frac{\left(\frac{D\cdot T_V}{T_g}\right)}{ln(10)\cdot\left(1-\frac{T_V}{T_g}\right)^2} \quad (5)$$

$$\Phi_g = \frac{(T_g - T_V)}{D\cdot T_V} \quad (6)$$

$$\alpha_g = \frac{1}{D\cdot T_V} \quad (7)$$

$$Ea_{Tg} = R\cdot\frac{\partial ln(\tau)}{\partial\left(\frac{1}{T}\right)} = \frac{R\cdot D\cdot T_V}{\left(1-\frac{T_V}{T_g}\right)^2} \quad (8)$$

The macromolecular origin of the relaxation mechanisms of the materials were studied with the Eyring theory [38]. Relaxations close to the zero-entropy line have an intramolecular origin and don't show cooperativity from neighbouring entities. In contrast, the relaxations with intermolecular origin involve interactions with neighbours, which leads to a cooperative effect and increases the activation energy of the mechanism.

The electron conductivity of the chitosan-lignin composites was investigated by analysing the real part of the conductivity (σ') with Jonscher's power law equation (Eq. (9)) [39]:

$$\sigma(\omega) = \sigma_{dc} + A\omega^n \tag{9}$$

where n is the frequency exponent in the range $0 < n \leq 1$, σ_{DC} is the direct current conductivity component and A is a preexponential factor. Theoretically at low frequencies the DC component is independent of the frequency and the electron conductivity (σ_{elec}) can be estimated from the plateau of σ' [40].

The proton conductivity (σ_{prot}) of the materials was calculated according to Eq. (10).

$$\sigma_{prot} = \frac{l}{R_0 \cdot A} \tag{10}$$

where l is the thickness of the membranes, A the area of the electrode in contact with the membrane, and R_0 the bulk resistance. For R_0 the value of the real impedance (Z') in the high frequency range is taken where log ($|Z|$) approaches a frequency-independent horizontal line and the phase angle (Φ) reaches its maximum in the Bode plot, according to $Z' = |Z| \cdot \cos(\Phi)$ [41].

3. Results and discussion

3.1. Chemical structure

The chemical structure of chitosan and the biocomposites containing different lignin fractions is presented by normalised FTIR spectra in Fig. 4.

Overall, the chitosan-lignin composites show similar absorbance at all the characterised bands, summarised in Table 1. Nevertheless, some slight differences can be seen at the bands of the hydroxyl, amino, and carboxylate groups, due to both the origin (KL or OL) and extraction step applied (EA or E) of the lignin.

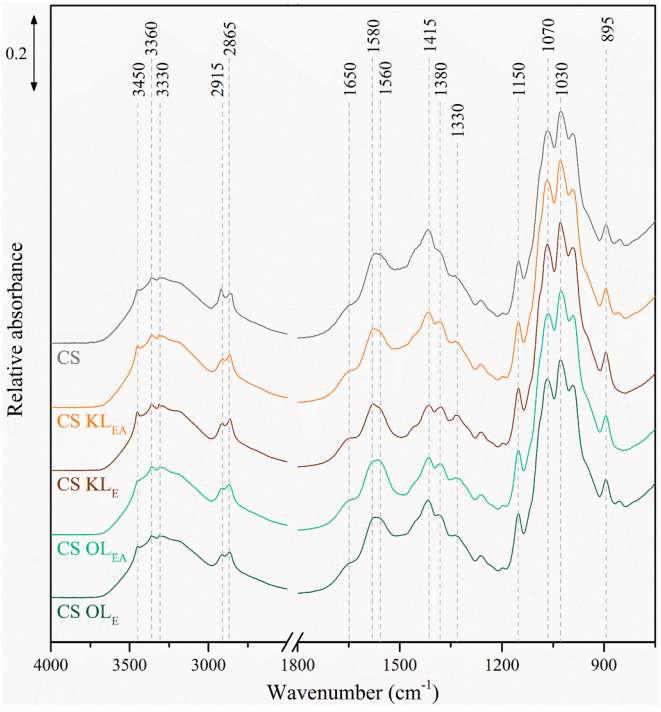

Fig. 4. FTIR spectra of chitosan (CS) and the composites CS KL_{EA}, CS KL_E, CS OL_{EA}, and CS OL_E.

Table 1
FTIR bands of chitosan.

Wavenumber (cm^{-1})	Designation	Reference
3450	xO-H	[42–45]
3360 + 3330	N-H	[43,45,46]
2915 + 2865	C-H of CH_2/CH_3	[42–45,47–50]
1650	C=O (Amide *I*)	[43–49,51–53]
1580	N-H of amino group and amide (Amide II)	[44,45,49]
1560	N-H of NH_3^+	[45,54–58]
1415	COO^-	[54,56,57]
1410 + 1380	CH_3 of amide	[45,49,53]
1330	C-H of CH_2	[42,43,47,48]
1150	Asymmetric C-O-C	[42,44,46–53]
1070 + 1030	C-O of β-1,4-glycosidic links	[42–44,46–50,53]
895	ring stretching	[42,43,48]

The membranes containing kraft lignin fractions (CS KL_{EA} & CS KL_E) show higher absorbance between 3500 and 3000 cm^{-1}, corresponding to the OH and the NH groups, compared to the membranes with organosolv fractions (CS OL_{EA} & CS OL_E). Also, among the composites with both lignin types (KL and OL) the fractions after extraction with ethyl acetate have a slightly higher absorbance between 3500 and 3000 cm^{-1} than after subsequent extraction with ethanol. These results are in agreement with Izaguirre et al. [19], who found higher phenolic OH contents in KL than in OL, which decrease after subsequent ethanol extraction.

Moreover, the composites show different absorption for the vibrations of the protonated amino group (NH_3^+) at 1560 cm^{-1} and the carboxylate ion ($-COO^-$) at 1415 cm^{-1} [54,56,57], with CS KL_{EA} and CS OL_E showing high absorbance.

3.2. Relaxation spectra of the composite membranes

3.2.1. Phenomenological analysis of the dielectric response

Fig. 5 represents the three-dimensional spectra of the imaginary part of the permittivity (ε'') as a function of frequency and temperature for all the chitosan-lignin composite membranes.

It can be seen from the 3D plots that the addition of the different lignin fractions affects the overall relaxation mechanisms and conductivity phenomena of the composite membranes due to alterations in the surface curvatures.

Fig. 6 represents the 2D isochronal plot of the material's loss factor (tan δ) of the chitosan-lignin composites as a function of temperature.

All materials show a complex dielectric relaxation spectrum with numerous relaxation mechanisms, that were labelled in order of increasing temperature as β, β_{wet}, and α-relaxation. In addition, at higher temperatures a σ-relaxation and a Maxwell Wagner Sillars (MWS) polarisation were observed.

The β-dielectric relaxation involves local motions of the main chain, related to fluctuations within the β-1,4-glycosidic bonds, as has been discussed in detail for various polysaccharides by Einfeldt et al. [59]. The β_{wet}-relaxation, first described by Pizzoli et al. [21], is attributed to orientational motions of a swollen mixed phase of both chitosan and water. The samples in this work have been dried prior to the measurement, but bound water can still remain in the composite structure after heating, also reported by Viciosa et al. [23]. This relaxation starts to vanish at temperatures near 100 °C when the water in the composites starts to evaporate. The α-relaxation represents the glass-rubber transition of the chitosan, which likewise disappears when the water evaporates.

The σ-relaxation is observed in the composites, due to the hopping motions of ions in the disordered structures of the biomaterial [23]. Owing to the evaporation of water, the conductivity phenomenon gets displaced to higher frequencies. The MWS polarisation at higher temperatures is usually found in inhomogeneous materials that form

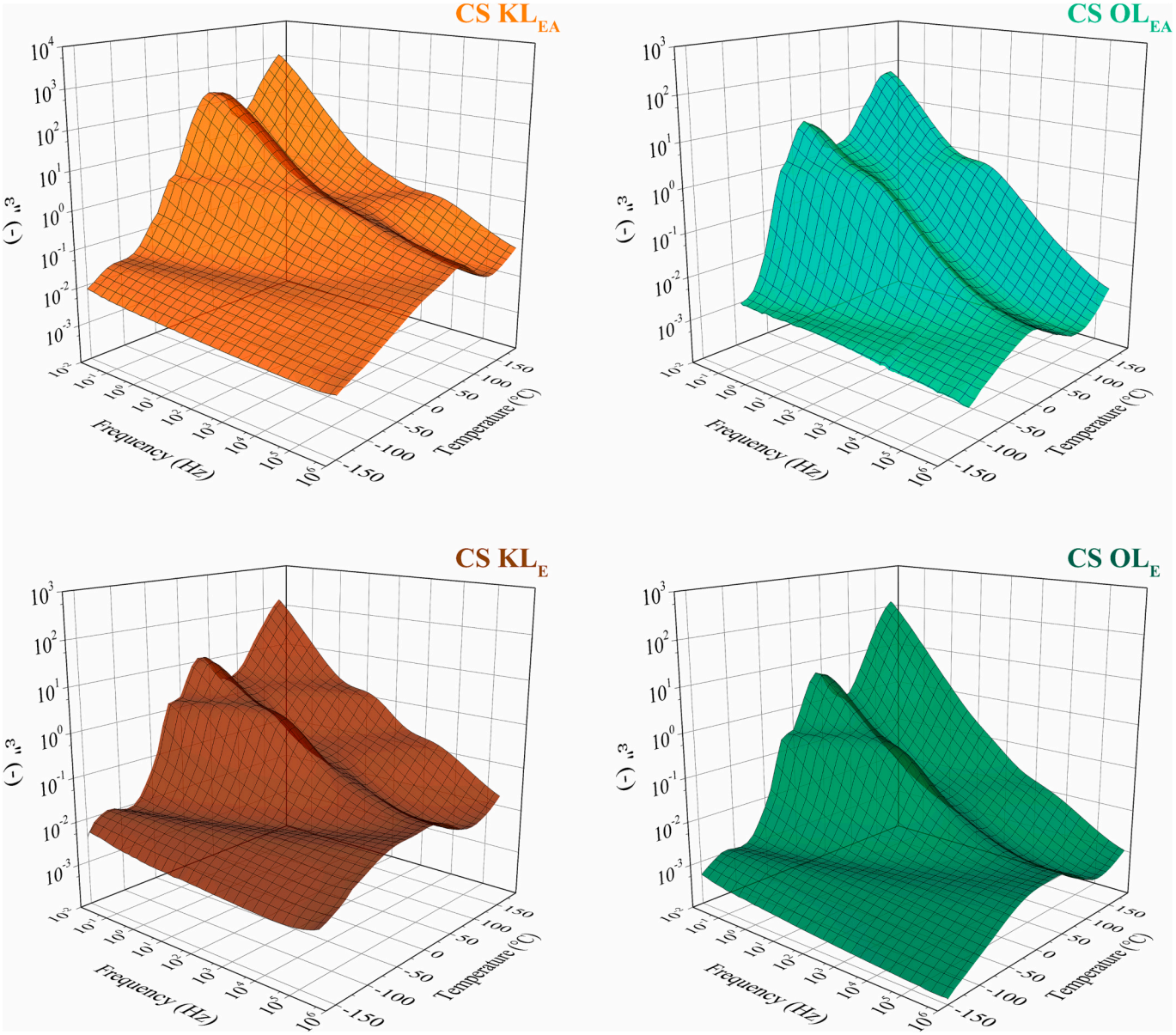

Fig. 5. 3D plots of the imaginary part of the permittivity (ε'') of the materials CS KL_{EA}, CS KL_{E}, CS OL_{EA}, and CS OL_{E}.

internal phase boundaries where charges can be blocked [23,24,60].

In order to analyse each of the above mentioned relaxations, the dielectric spectra (ε'') were deconvoluted with Havriliak–Negami (HN) functions and the relaxation times obtained [32,33].

Fig. 7 shows the Eyring plot of the chitosan-lignin composites with all their molecular relaxations and conductivity phenomena to analyse their non-cooperative or cooperative origin.

Generally, the local motions are not influenced by neighbouring entities [38], although all the relaxation mechanisms of the composites in this study seem to have a cooperative origin, as they show a deviation from the zero-entropy line. The addition of the different lignin fractions influences the relaxation mechanisms, due to its numerous functional groups that can interact with the chitosan chain. On the other hand, the conductivity phenomena show no considerable deviation from the zero-entropy line. Overall, the relaxations of the composites with lignin fractions after extraction with ethyl acetate show higher cooperativity compared after extraction with ethanol.

3.2.2. *Analysis of the low-temperature relaxations*

As mentioned earlier, all the chitosan-lignin composites show a β- and a β_{wet}-relaxation at low temperatures. In order to study these relaxation mechanisms directly, an Arrhenius map is plotted in Fig. 8.

The β-relaxation, referring to fluctuations of the glycosidic bonds, appears at low temperatures and shows a linear dependency between the relaxation time and temperature. Consequently, this relaxation was modelled with the Arrhenius equation and the results are summarised in Table 2.

Einfeldt et al. have explained this β-relaxation in detail for various polysaccharides with glycosidic links, including chitosan, and found apparent activation energies (E_a) around 45 kJ·mol^{-1} [59]. Other authors likewise discovered the β-relaxation of pure chitosan with activation energies between 46.0 and 49.0 kJ·mol^{-1} [21,23–25]. The results of the Arrhenius fit in Table 2 demonstrate that all the chitosan-lignin composites exhibit higher activation energies between 62.7 and 68.0 kJ·mol^{-1}. As shows Fig. 2, lignin's polar groups can form hydrogen bonds with the chitosan chains and restrict their movement, leading to

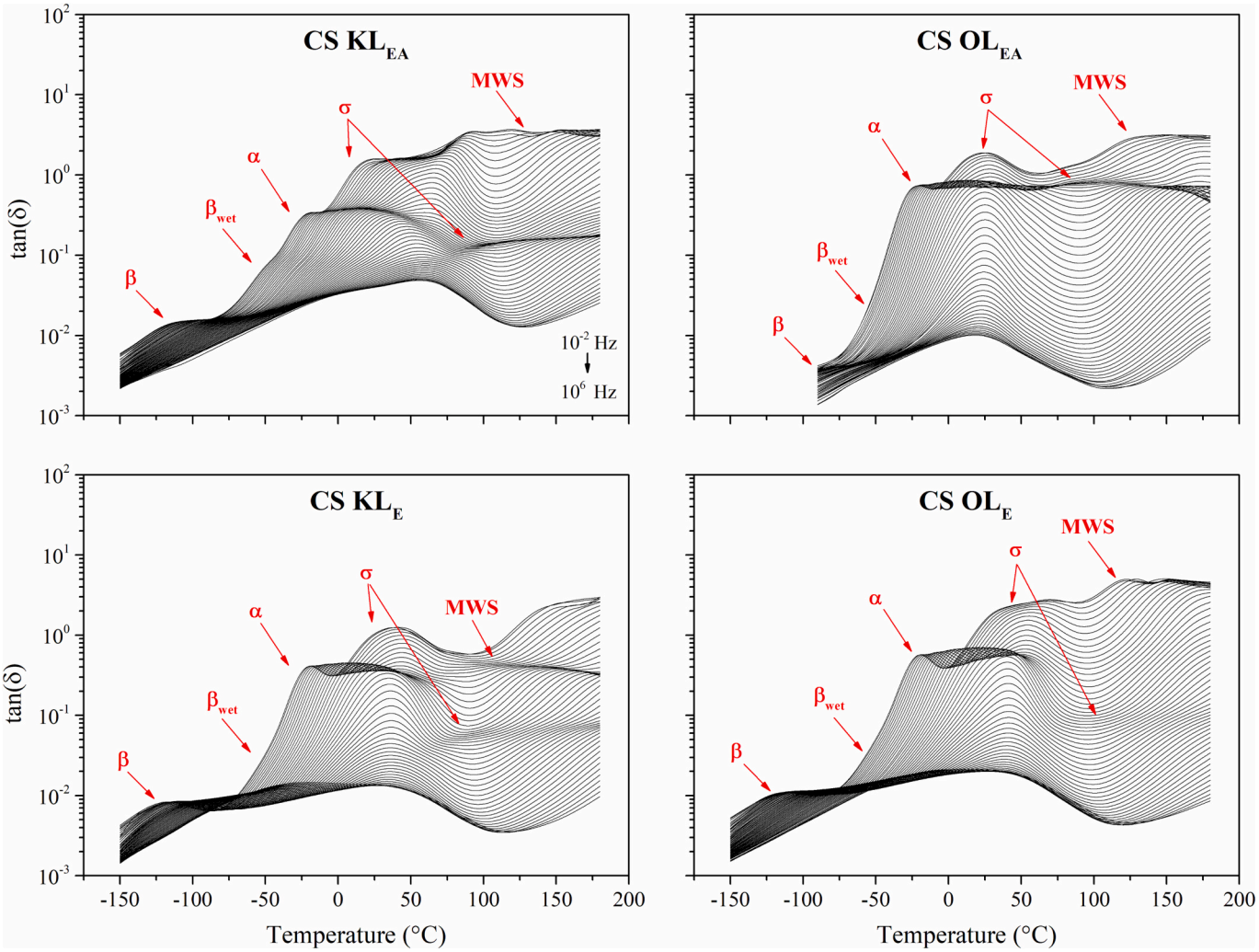

Fig. 6. Isochronal plots of tan(δ) of CS KL_{EA}, CS KL_E, CS OL_{EA}, and CS OL_E in the temperature range between −150 °C and 180 °C.

higher activation energies. This intermolecular connection effect of the lignin filler explains the small cooperative origin of the β-relaxation previously observed in the Eyring plot.

Even though the β-relaxations of the chitosan-lignin composites have comparable activation energies, they are displaced in temperature depending on the extraction step applied to the lignin types, as shown in both Fig. 8 and Table 2. The relaxations of the composites with KL and OL after ethyl acetate extraction occur at higher temperatures than those of the composites with lignin after ethanol extraction.

The lignin fractions after the first extraction with ethyl acetate consist of molecules with low molecular weight (KL_{EA}: M_n/M_w = 702/2422 Da; OL_{EA}: M_n/M_w = 470/1772 Da), compared to the lignin fractions after subsequent ethanol extraction (KL_E: M_n/M_w = 1545/5678 Da; OL_E: M_n/M_w = 919/2237 Da), as the small components are easily soluble in the first step [19]. The small lignin molecules can be distributed more evenly and create stronger interactions with the chitosan chains. In addition, as previously observed in FTIR studies, the composites with KL have more hydroxy groups than the composites with OL, which decreases slightly for both types after subsequent lignin extraction with ethanol. The higher number of hydroxyl groups indicate stronger hydrogen bonding of the lignin filler with the chitosan chain. Therefore, higher temperatures are required to initiate the β-relaxation of the chitosan composites containing lignin fractions after ethyl acetate extraction.

At slightly higher temperatures, all chitosan-lignin composites show a β_{wet}-relaxation, which presents a linear region at lower frequencies and displays a curvature at higher frequencies. The curving is presumed to be due to the previously mentioned evaporation of water, which starts around 60 °C. Since the β_{wet}-relaxation is attributed to motions of a mixed phase of both chitosan and bound water, it is clearly influenced by the state of the water. As the temperature increases, the hydrogen links between bound water and chitosan may break and the structure of the swollen phase changes. Thus, the complex is less restricted, smaller and the frequency required to induce the movement lower, explaining the curvature. The linear region of the β_{wet}-relaxation process was modelled using the Arrhenius equations and the results are summarised in Table 3.

Nogales et al. and Viciosa et al. found activation energies of 71.0 and 62.5 kJ·mol^{-1} for the β_{wet}-relaxation of pure chitosan, respectively [22,24]. In this study, the activation energies of the β_{wet}-relaxation of all the chitosan-lignin composites were found between 95.6 and 127.4 kJ·mol^{-1}. Pizzoli et al. suggested that the β_{wet}-relaxation could not only arise through water absorption, but also when other low-molecular weight molecules are incorporated [21]. Therefore, similar to the β-relaxation, the higher activation energies of the β_{wet}-relaxation are due to the incorporation of lignin, which together with bound water form a complex phase that exhibits cooperative behaviour. The relaxation seems to depend on the size of the lignin molecules in the composite,

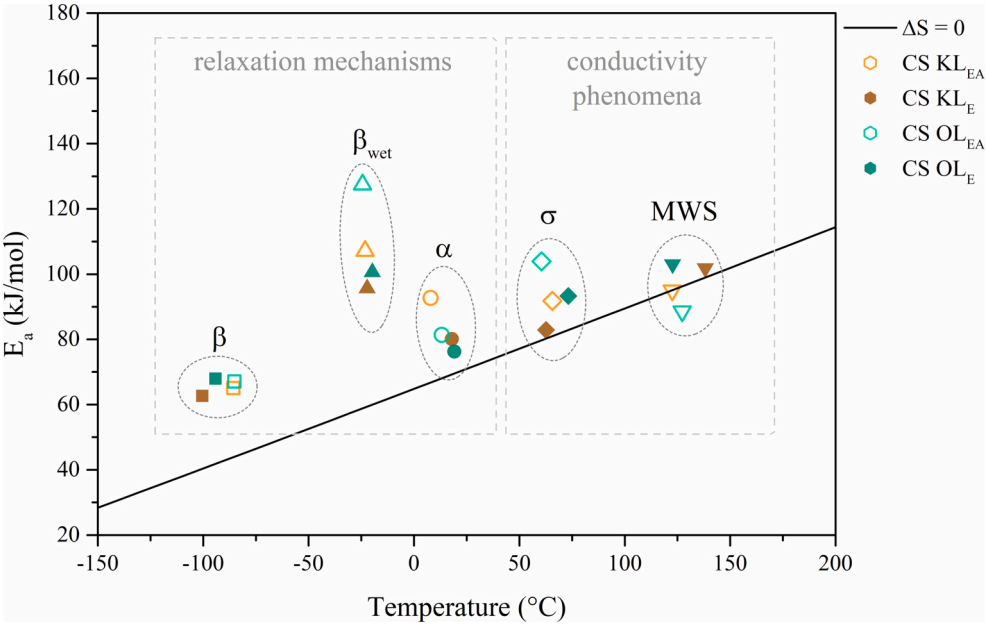

Fig. 7. Eyring plot of the composites CS KL_{EA}, CS KL_E, CS OL_{EA}, and CS OL_E at 1 Hz.

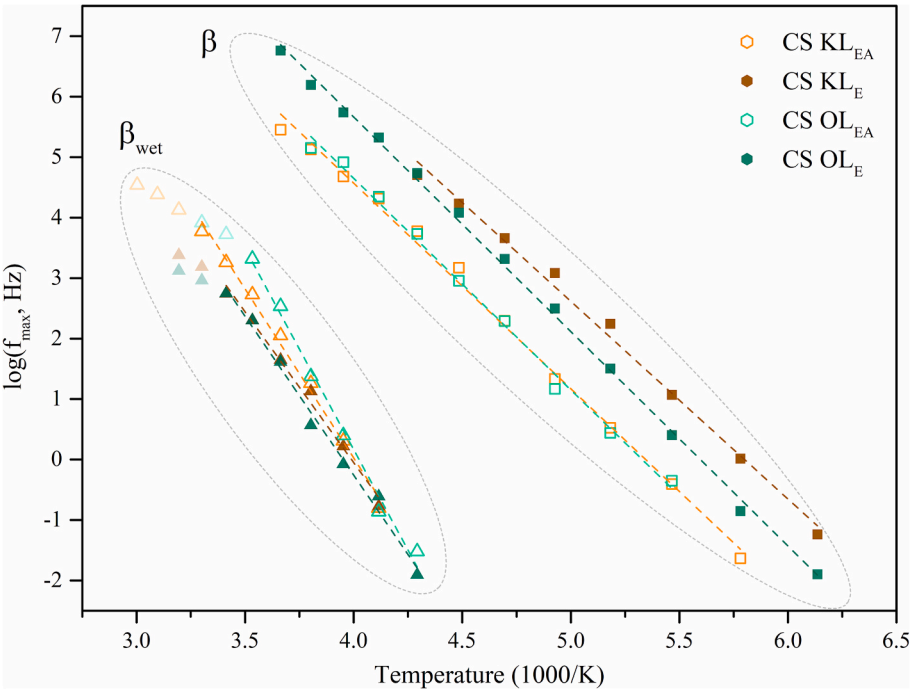

Fig. 8. Arrhenius map of the β- and β_{wet}-relaxation of CS KL_{EA}, CS KL_E, CS OL_{EA}, and CS OL_E.

with the fractions having the lowest molar mass showing the highest activation energy. As previously explained, the smaller lignin molecules can create stronger intermolecular connections, due to a more evenly distribution in the composite.

3.2.3. *Analysis of the α-relaxations*

In the literature it has been reported that in chitosan films without any water the glass transition could not be observed [26,29]. In the studied chitosan-lignin composites the α-relaxation was found between −10 and 70 °C at low frequencies, as it can be appreciated in the Arrhenius map in Fig. 9. The glass transition of chitosan diminishes after the water content decreases at temperatures towards 100 °C, which is attributed to the evaporation of the bound water.

The relationship between the relaxation time of the α-relaxations and the temperature shows a non-linear behaviour, as shows the Arrhenius map in Fig. 9. Thus, the α-relaxations of the chitosan-lignin composites were adjusted to the VFTH equation, and the results of the fit are summarised in Table 4. From the VFTH fit further parameters can be obtained, such as the fragility index m, the free volume coefficient Φ_g, the thermal expansion coefficient α_g, and the apparent activation energy

Table 2
Arrhenius fit values of the β-relaxation of the samples CS KL_E, CS KL_{EA}, CS OL_E, and CS OL_{EA}.

	β-relaxation		
	E_a (kJ·mol^{-1})	T_{max} at 1 Hz (°C)	R^2
CS KL_{EA}	65.1	−85.7	0.996
CS KL_E	62.7	−100.4	0.994
CS OL_{EA}	67.1	−85.2	0.995
CS OL_E	68.0	−94.2	0.997

Table 3
Arrhenius fit values of the β_{wet}-relaxation of the samples CS KL_E, CS KL_{EA}, CS OL_E, and CS OL_{EA}.

	β_{wet}-relaxation		
	E_a (kJ·mol^{-1})	T_{max} at 1 Hz (°C)	R^2
CS KL_{EA}	107.1	−23.1	0.993
CS KL_E	95.6	−22.2	0.991
CS OL_{EA}	127.4	−24.4	0.991
CS OL_E	100.6	−19.7	0.991

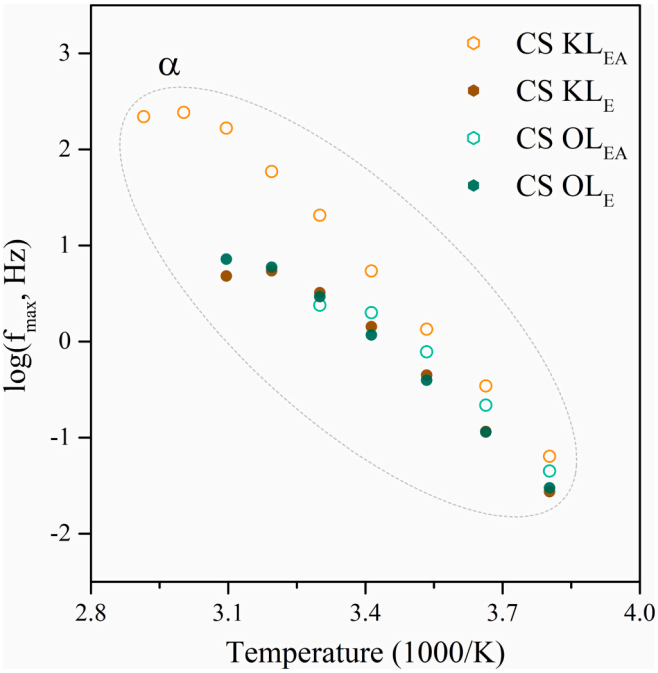

Fig. 9. Arrhenius map of the α-relaxation of CS KL_{EA}, CS KL_E, CS OL_{EA}, and CS OL_E.

Ea_{Tg}.

The fragility index (m) provides information on how the properties of the materials change when approaching the glass transition. Fragile materials with low fragility indices ($16 < m < 100$) show abrupt changes in their physical properties, while strong materials ($100 < m < 200$) show a smooth transition from the glassy to the rubbery state [37]. All the chitosan-lignin composites show low fragility indices (m) between 15.3 and 37.7.

The composites prepared with lignin fractions, which have more hydroxyl groups exhibit higher fragility. The composites with lignin fractions extracted with ethanol decreases the fragility in both type of lignin. The lignin fraction KL_{EA} has the highest content of hydroxy groups and a low molecular weight [19] and therefore is most

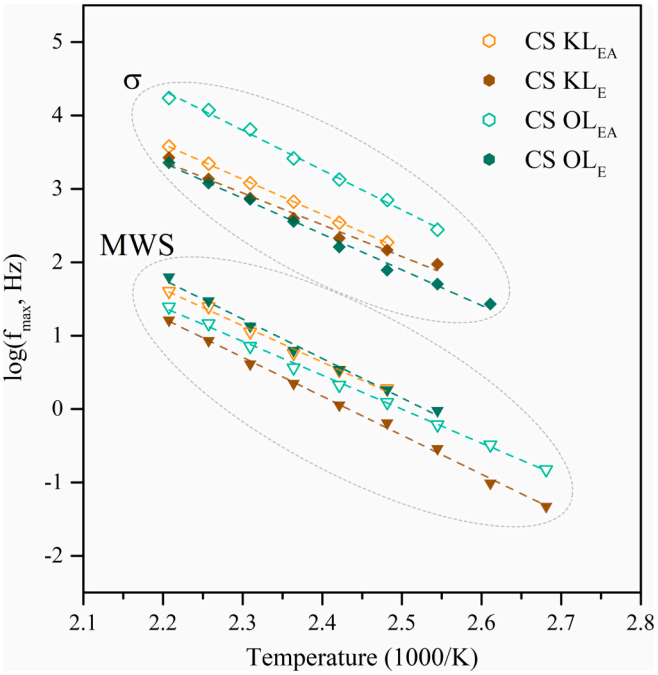

Fig. 10. Arrhenius map of the σ-relaxation and MWS-polarisation of CS KL_{EA}, CS KL_E, CS OL_{EA}, and CS OL_E.

Table 5
Arrhenius fit values of the σ-relaxation and the MWS-polarisation of the samples CS KL_E, CS KL_{EA}, CS OL_E, and CS OL_{EA}.

	σ-relaxation		
	E_a (kJ·mol^{-1})	T_{max} at 1 Hz (°C)	R^2
CS KL_{EA}	91.8	65.7	0.999
CS KL_E	82.9	62.7	0.983
CS OL_{EA}	103.9	60.5	0.995
CS OL_E	93.3	73.3	0.993

	MWS-polarisation		
	E_a (kJ·mol^{-1})	T_{max} at 1 Hz (°C)	R^2
CS KL_{EA}	95.0	122.6	0.993
CS KL_E	101.8	138.2	0.998
CS OL_{EA}	88.6	127.3	0.998
CS OL_E	103.0	122.7	0.992

Table 4
VFTH fit parameters and derived fragility parameters of the α-relaxation of CS KL_{EA}, CS KL_E, CS OL_{EA}, and CS OL_E.

	α-relaxation								
	VFTH fit					Fragility parameters			
	$Log\ f_0$ (Hz)	D	T_V (K)	R^2	T_g (°C)	m	Φ_g	$\alpha_g \cdot 10^4$ (K^{-1})	Ea_{Tg} (kJ·mol^{-1})
CS KL_{EA}	6.34 ± 1.13	3.64 ± 2.51	220.5 ± 24.7	0.995	−2.7	37.7	0.062	12.46	195.3
CS KL_E	3.83 ± 0.48	2.23 ± 0.80	219.6 ± 10.2	0.997	−3.6	22.9	0.102	20.42	118.4
CS OL_{EA}	3.52 ± 0.60	2.33 ± 0.94	209.3 ± 10.1	0.993	−13.9	22.0	0.103	20.51	109.0
CS OL_E	3.30 ± 0.88	1.29 ± 1.16	237.4 ± 22.9	0.979	14.3	15.3	0.163	32.65	84.1

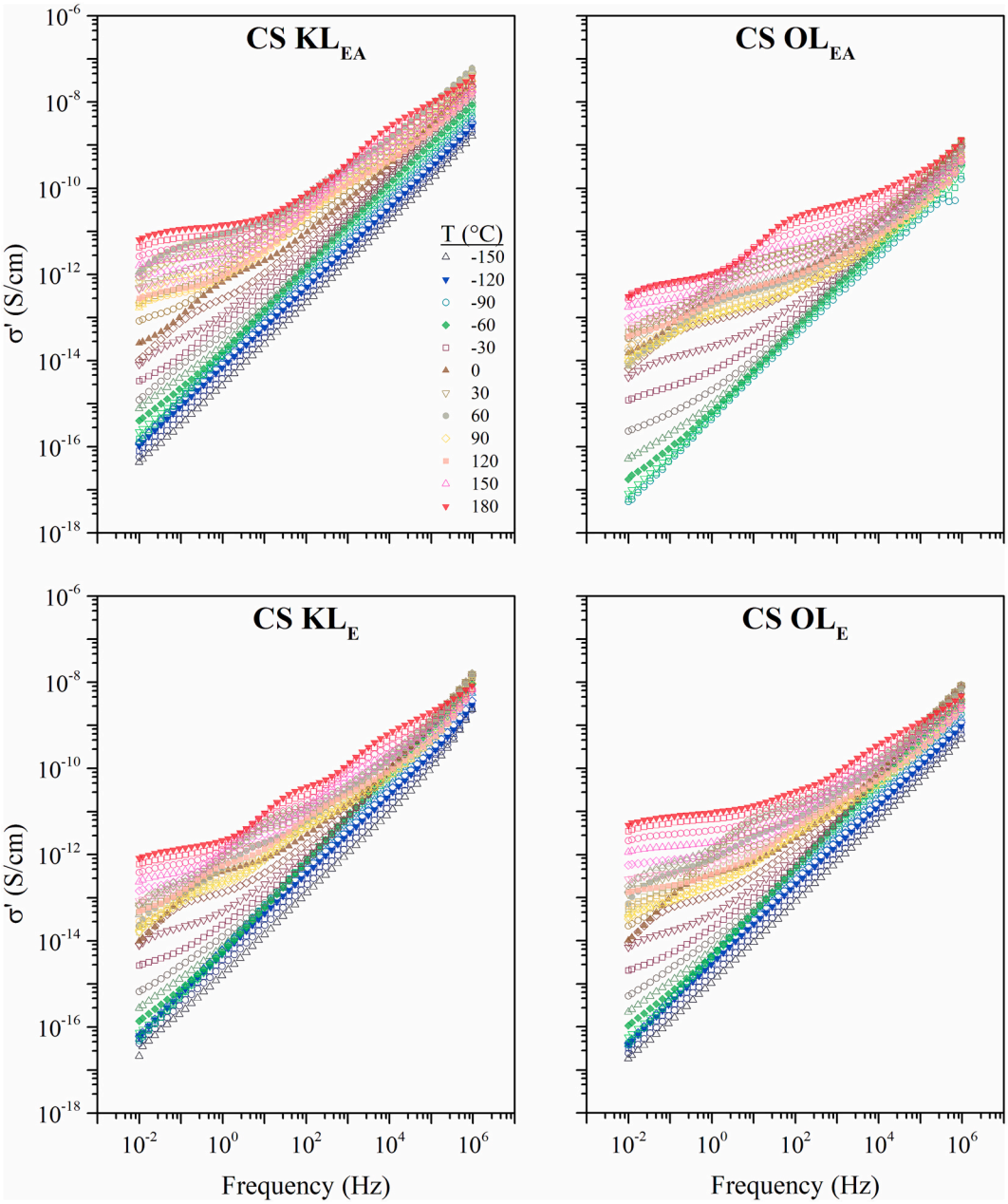

Fig. 11. Real part of the conductivity (σ') of CS KL_{EA}, CS KL_{E}, CS OL_{EA}, and CS OL_{E}.

Table 6
Jonscher fit of the real part of conductivity (σ') of CS KL_{EA}, CS KL_{E}, CS OL_{EA}, and CS OL_{E}.

	Temperature (°C)	σ_0 (S·cm^{-1})	A	n	R^2
CS KL_{EA}	120	$3.1\cdot10^{-13}$	$4.7\cdot10^{-14}$	0.70	0.999
	140	$1.0\cdot10^{-12}$	$7.4\cdot10^{-14}$	0.70	0.999
	160	$3.6\cdot10^{-12}$	$1.0\cdot10^{-13}$	0.72	0.999
CS KL_{E}	120	$3.4\cdot10^{-14}$	$3.2\cdot10^{-14}$	0.83	0.999
	140	$1.5\cdot10^{-13}$	$3.0\cdot10^{-14}$	0.91	0.999
	160	$4.6\cdot10^{-13}$	$2.9\cdot10^{-14}$	0.94	0.998
CS OL_{EA}	120	$3.0\cdot10^{-14}$	$1.7\cdot10^{-14}$	0.68	0.999
	140	$1.0\cdot10^{-13}$	$2.0\cdot10^{-14}$	0.76	0.997
	160	$3.6\cdot10^{-13}$	$1.8\cdot10^{-14}$	0.86	0.998
CS OL_{E}	120	$1.5\cdot10^{-13}$	$1.6\cdot10^{-14}$	0.65	0.997
	140	$7.9\cdot10^{-13}$	$1.6\cdot10^{-14}$	0.71	0.999
	160	$3.5\cdot10^{-12}$	$2.8\cdot10^{-14}$	0.70	0.999

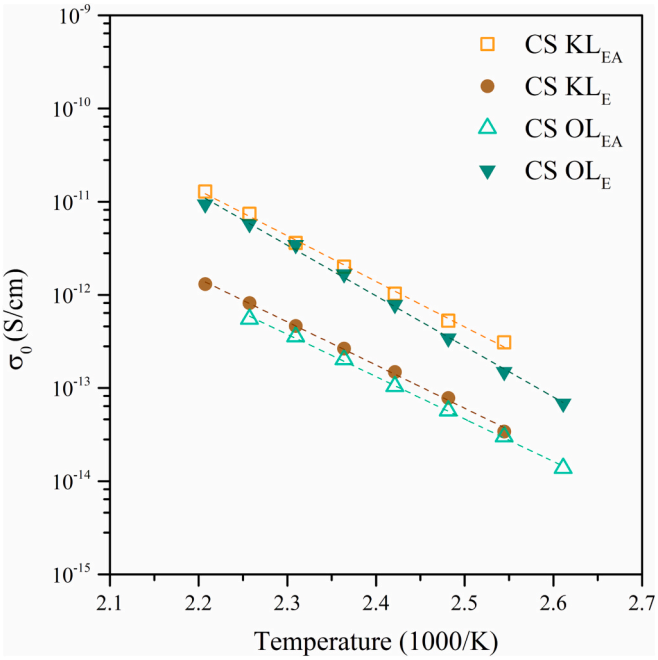

Fig. 12. Arrhenius map of the electron conductivity (σ_0) of CS KL$_{EA}$, CS KL$_{E}$, CS OL$_{EA}$, and CS OL$_{E}$.

Table 7
Arrhenius fit and activation energies of the electron conductivity of CS KL$_{EA}$, CS KL$_{E}$, CS OL$_{EA}$, and CS OL$_{E}$.

	Intercept	Slope	E_a (kJ·mol^{-1})	R^2
CS KL$_{EA}$	−0.13	−4.89	93.6	0.996
CS KL$_{E}$	−1.62	−4.64	88.8	0.997
CS OL$_{EA}$	−1.95	−4.55	87.1	0.999
CS OL$_{E}$	1.00	−5.43	104.0	0.997

compatible with the chitosan matrix resulting in a high fragility of the composite. Therefore, the composite CS KL$_{EA}$ results in a compact structure with a low free volume coefficient Φ_g, low thermal expansion coefficient α_g and a high activation energy Ea_{Tg}.

3.2.4. Evaluation of the conductivity phenomena

In the dielectric spectra of the chitosan-lignin composites the two processes at elevated temperatures were assigned to conductivity phenomena. Fig. 10 shows the Arrhenius map of both the σ-relaxation and the MWS-polarisation.

Both processes show a linear temperature dependency, which can be appreciated in Fig. 10. Consequently, they are described with the Arrhenius equation with their results being summarised in Table 5. The σ-relaxation of the chitosan-lignin composites shows apparent activation energies between 91.8 and 103.9 kJ·mol^{-1}. These are typical values reported for σ-relaxations of chitosan based materials [21,23–25,28,29,60].

The process at high temperatures and low frequencies was assigned to MWS interfacial polarisation. The process of the composites with lignin fractions after ethyl acetate extraction compared to the composite with lignin fractions after subsequent ethanol extraction have lower apparent activation energies.

3.2.4.1. Electron conductivity. Furthermore, the electron conductivity of the chitosan-lignin composites is investigated by using the real part of the conductivity (σ'), which was plotted as a function of frequency and temperature, as shown in Fig. 11.

The conductivity progression of the materials can be described according Jonscher's power law [39]. Ideally, at high frequencies the power law feature ($\sigma \sim \omega^n$) can be observed, and the DC part (σ_{DC}) becomes almost negligible, resulting in a linearly conductivity increase as a function of frequency. On the other hand, at low frequencies the curve for the conductivity is frequency independent and shows a plateau, representing the bulk conductivity (σ_0) or electron conductivity (σ_{elec}).

In Fig. 11 it can be seen that the conductivity of the chitosan-lignin composites has curvatures at certain temperatures, indicating that the conductivity is influenced by charge mitigation processes and relaxation phenomena.

The plateau visible at high temperatures were adjusted according to Jonscher's power law and the results for the chitosan-lignin composites at three exemplary temperatures are listed in Table 6.

All the studied chitosan-lignin composites exhibit low conductivities between 10^{-14} and 10^{-11} S·cm^{-1} and are thus regraded electric insulators [61]. All the composites show high values of the exponential component n between 0.6 and 1.0, which is a qualitative parameter that gives information about the morphological texture. Values near 1 describe materials with ideal charge-conducting paths, while values lower than 0.5 describe a network with high levels of tortuosity [62]. The membranes CS KL$_{E}$ and CS OL$_{EA}$ show higher n-values, indicating better long-range pathways for electron conduction.

To further examine the conductivity mechanism of the composite materials, their thermal activation and temperature dependency were acquired. Fig. 12 shows the Arrhenius map of the conductivity mechanism and Table 7 summarises the results from the Arrhenius fit.

The composite membranes show activation energies around 95 kJ·mol^{-1}, similar to the values obtained for the σ-relaxation and MWS polarisation, demonstrated in Table 5. The conductivity process of the membrane CS KL$_{EA}$ and CS OL$_{E}$ are located at higher frequencies.

3.2.4.2. Proton conductivity. Lastly, the proton conductivity (σ_{prot}) of the chitosan-lignin composites was calculated from the Bode plots, illustrated in Fig. 13.

The Bode plots of the chitosan-lignin composites show a curve progression with two curvatures. The process on the left referrs to a relaxation influencing the conductivity and the peak on the right at high frequencies to the bulk resistency (R_0), used for the caluclation of the proton conductivtiy. Fig. 14 plots the calculated proton conductivity (σ_{prot}) of the chitosan-lignin composites between 20 and 80 °C.

The proton conductivity of the composites as a function of temperature shows the same curve progressions, experiencing an increase until reaching a maximum value around 60 °C and afterwards declining. The increase in conductivity arises from the promoted activity of hydronium ions and chain motion [63,64]. The decrease after 60 °C is supposed to be due to starting evaporation of bound water. In particular the vehicle mechanism is inhibited, in which protons react with water to form hydronium ions, and then diffuse through the membrane.

The CS KL$_{E}$ and CS OL$_{EA}$ composites exhibit the highest proton conductivity (0.12/0.11 mS·cm^{-1}) and at the same time the lowest electron conductivity (12.2/3.7·10^{-10} mS·cm^{-1}). These properties are desirable for fuel cell applications.

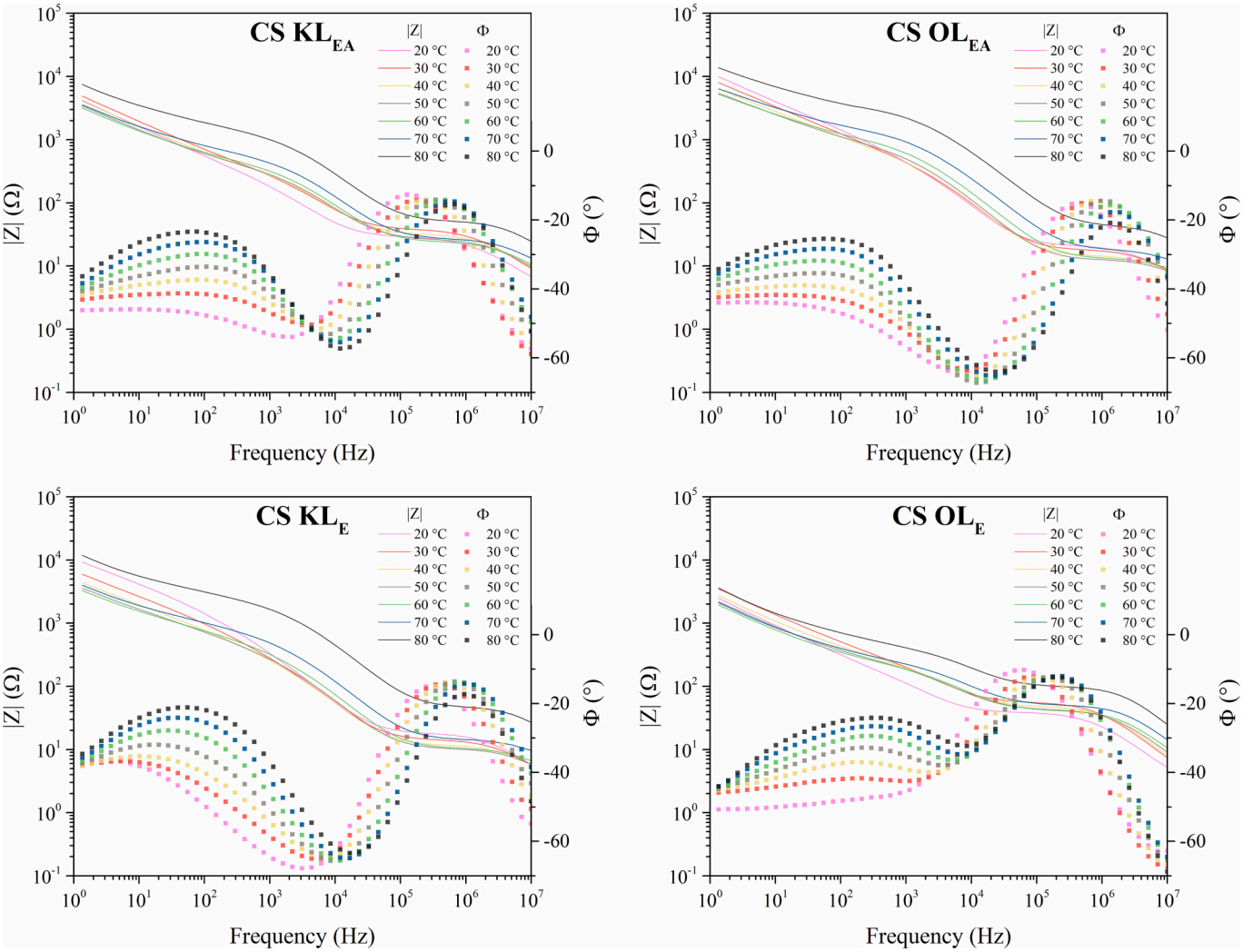

Fig. 13. Bode plot of impedance ($|Z|$) and phase angle (Φ) of CS KL_{EA}, CS KL_{E}, CS OL_{EA}, and CS OL_{E}.

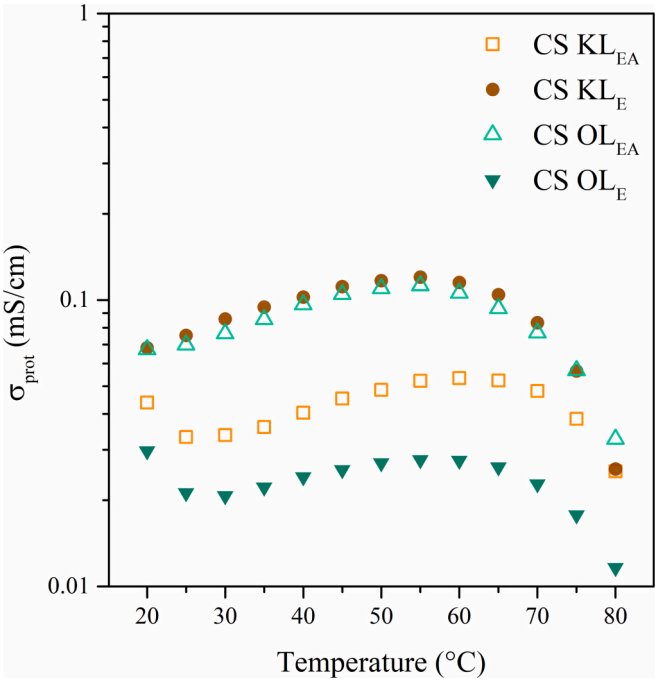

Fig. 14. Proton conductivity (σ_{prot}) of wet CS KL_{EA}, CS KL_{E}, CS OL_{EA}, and CS OL_{E} between 20 and 80 °C.

4. Conclusions

Adding a small percentage (1%) of fractioned lignin to chitosan, the dielectric spectrum has the same five processes of neat chitosan, including three relaxation mechanisms (β, β_{wet}, and α relaxation) and two phenomena related to the conductivity (σ relaxation and MWS polarisation).

The lignin fractions and the chitosan chains can interact through hydroxyl ($^{-}$OH), carboxylate (-COO^{-}) and amino (NH_3^{+}) groups, that together with the water content, and the differences in the molecular mass of the lignin, are responsible for the differences observed in the relaxation spectra and conductivity properties.

Depending on the type of lignin (kraft or organosolv) and the extraction process applied (ethyl acetate or subsequent ethanol), the characteristic functional groups, molar mass etc., above mentioned, are modified, so that bio-composites with suitable properties can be obtained. The kraft lignin (KL) fraction has higher content of OH groups than organosolv lignin (OL) fraction and it can build stronger bonds with the chains. In addition, the lignin fractions of both KL and OL possess slightly more OH groups after ethyl acetate extraction than subsequent ethanol ones.

This intermolecular interaction between the chains restricts the molecular motion, including a cooperativity component, even in the β and β_{wet} relaxations, which origin is a local motion. Thus, both relaxations exhibit higher temperature-peak and activation energies due to stronger internal hydrogen bonding.

The β_{wet} and α relaxations strongly depend on the water content, specially α relaxations, which cooperative motions could be restricted if the temperature reaches 100 °C.

The fractions obtained through ethyl acetate extraction have lower molecular weights, which allows for more uniform distribution in the composite membrane, leading to stronger intermolecular effects. Consequently, the β_{wet}-relaxation of the CS OL_{EA} bio-composite membrane shows the highest activation energy due to the lowest molecular mass of the OL_{EA} fraction.

All the chitosan-lignin composites are fragile materials. The composite containing more polar functional groups are more fragile, showing a lower free volume coefficient than the others. The bio-composite membrane with KL_{EA} fraction has a high activation energy (at each temperature) related to the α relaxation, a compact structure with low free volume coefficient, and low thermal expansion.

CS KL_E and CS OL_{EA} bio-composite membranes exhibit low electron and high proton conductivity, which could be applied as electrolytes in fuel cells, although the absolute values of proton conductivity should be improved.

CRediT authorship contribution statement

M.H. Wolf: Data curation, Formal analysis, Investigation, Methodology, Visualization, Writing – original draft. **N. Izaguirre:** Investigation, Resources. **B. Pascual-José:** Conceptualization, Data curation, Formal analysis, Validation, Writing – original draft. **R. Teruel-Juanes:** Investigation, Methodology. **J. Labidi:** Funding acquisition, Project administration, Resources, Supervision. **A. Ribes-Greus:** Funding acquisition, Project administration, Resources, Supervision, Writing – review & editing.

Declaration of competing interest

The authors declare the following financial interests/personal relationships which may be considered as potential competing interests:

A. Ribes-Greus reports financial support was provided by Spanish Ministry of Science and Innovation. A. Ribes-Greus reports financial support was provided by Government of Valencia. M.H. Wolf reports financial support was provided by Spanish Ministry of Universities. R. Teruel-Juanes reports financial support was provided by Universitat Politècnica de València. N. Izaguirre reports financial support was provided by Basque Government.

Data availability

The data supporting the findings of this study cannot be shared at this time as the data also forms part of an ongoing study.

Acknowledgements

This study forms part of the Advanced Materials programme and was supported by the Spanish Ministry of Science and Innovation with funding from the European Union NextGenerationEU (PRTR-C17.11) and by the Generalitat Valenciana as project INNOMAT-H2 (MFA/2022/041). The authors also thank the Spanish Ministry of Universities for the pre-doctoral FPU grant of M.H. Wolf (FPU21/00853), the Basque Government for the grant of N. Izaguirre (PIF19-183) and the Universitat Politècnica de València for the PAID-10-19 SUB.1 grant of R. Teruel-Juanes (SP20190049). The authors are also grateful to Karel Beirnaert for experimental assistance in material characterisation.

References

[1] O. Gómez-Jimenéz-Aberatsuri, Eco-friendly materials for chemical products manufacturing: adhesives dervied from biomass and renewable resources, in: Handb. Ecomater, 2019, pp. 1937–1952, https://doi.org/10.1007/978-3-319-68255-6.

[2] M. Yadav, P. Goswami, K. Paritosh, M. Kumar, N. Pareek, V. Vivekanand, Seafood waste: a source for preparation of commercially employable chitin/chitosan materials, Bioresour. Bioprocess. 6 (2019), https://doi.org/10.1186/s40643-019-0243-y.

[3] M. Rinaudo, Chitin and chitosan: properties and applications, Prog. Polym. Sci. 31 (2006) 603–632, https://doi.org/10.1016/j.progpolymsci.2006.06.001.

[4] N.A. Mohamad Aini, N. Othman, M.H. Hussin, K. Sahakaro, N. Hayeemasae, Lignin as alternative reinforcing filler in the rubber industry: a review, Front. Mater. 6 (2020), https://doi.org/10.3389/fmats.2019.00329.

[5] J.H. Lora, Industrial commercial lignins: sources, properties and applications, in: Monomers, Polym. Compos. from Renew. Resour, 2008, pp. 225–241, https://doi.org/10.1016/B978-0-08-045316-3.00010-7.

[6] I. Haq, P. Mazumder, A.S. Kalamdhad, Recent advances in removal of lignin from paper industry wastewater and its industrial applications – a review, Bioresour. Technol. 312 (2020) 123636, https://doi.org/10.1016/j.biortech.2020.123636.

[7] S. Sohni, R. Hashim, H. Nidaullah, J. Lamaming, O. Sulaiman, Chitosan/nano-lignin based composite as a new sorbent for enhanced removal of dye pollution from aqueous solutions, Int. J. Biol. Macromol. 132 (2019) 1304–1317, https://doi.org/10.1016/j.ijbiomac.2019.03.151.

[8] S.S. Vedula, G.D. Yadav, Wastewater treatment containing methylene blue dye as pollutant using adsorption by chitosan lignin membrane: development of membrane, characterization and kinetics of adsorption, J. Indian Chem. Soc. 99 (2022) 100263, https://doi.org/10.1016/j.jics.2021.100263.

[9] K. Ravishankar, M. Venkatesan, R.P. Desingh, A. Mahalingam, B. Sadhasivam, R. Subramaniyam, R. Dhamodharan, Biocompatible hydrogels of chitosan-alkali lignin for potential wound healing applications, Mater. Sci. Eng. C 102 (2019) 447–457, https://doi.org/10.1016/j.msec.2019.04.038.

[10] R. Wang, S. Gao, Z. Yang, Y. Li, W. Chen, B. Wu, W. Wu, Engineered and laser-processed chitosan biopolymers for sustainable and biodegradable triboelectric power generation, Adv. Mater. 30 (2018), https://doi.org/10.1002/adma.201706267.

[11] W. Wang, B. Shan, L. Zhu, C. Xie, C. Liu, F. Cui, Anatase titania coated CNTs and sodium lignin sulfonate doped chitosan proton exchange membrane for DMFC application, Carbohydr. Polym. 187 (2018) 35–42, https://doi.org/10.1016/j.carbpol.2018.01.078.

[12] Y. Pi, X. Wu, Z. Zheng, L. Ma, T. Wang, Chitosan-lignin carbon framework-encapsulated Cu catalyst facilitates base-free hydrogen evolution from methanol/water†, Catal. Sci. Technol. 12 (2022) 1941–1949, https://doi.org/10.1039/d1cy01698a.

[13] Y. Chai, Y. Wang, B. Li, W. Qi, R. Su, Z. He, Microfluidic synthesis of lignin/chitosan nanoparticles for the pH-responsive delivery of anticancer drugs, Langmuir 37 (2021) 7219–7226, https://doi.org/10.1021/acs.langmuir.1c00778.

[14] X. Ji, M. Guo, Preparation and properties of a chitosan-lignin wood adhesive, Int. J. Adhes. Adhes. 82 (2018) 8–13, https://doi.org/10.1016/j.ijadhadh.2017.12.005.

[15] F.G. Calvo-Flores, J.A. Dobado, Lignin as renewable raw material, ChemSusChem 3 (2010) 1227–1235, https://doi.org/10.1002/cssc.201000157.

[16] S.J. Xiong, S.J. Zhou, H.H. Wang, H.M. Wang, S. Yu, L. Zheng, T.Q. Yuan, Fractionation of technical lignin and its application on the lignin/poly-(butylene adipate-co-terephthalate) bio-composites, Int. J. Biol. Macromol. 209 (2022) 1065–1074, https://doi.org/10.1016/j.ijbiomac.2022.04.065.

[17] A. Tagami, C. Gioia, M. Lauberts, T. Budnyak, R. Moriana, M.E. Lindström, O. Sevastyanova, Solvent fractionation of softwood and hardwood kraft lignins for more efficient uses: compositional, structural, thermal, antioxidant and adsorption properties, Ind. Crop. Prod. 129 (2019) 123–134, https://doi.org/10.1016/j.indcrop.2018.11.067.

[18] N. Izaguirre, E. Robles, R. Llano-Ponte, J. Labidi, X. Erdocia, Fine-tune of lignin properties by its fractionation with a sequential organic solvent extraction, Ind. Crop. Prod. 175 (2022) 114251, https://doi.org/10.1016/j.indcrop.2021.114251.

[19] N. Izaguirre, O. Gordobil, E. Robles, J. Labidi, Enhancement of UV absorbance and mechanical properties of chitosan films by the incorporation of solvolytically fractionated lignins, Int. J. Biol. Macromol. 155 (2020) 447–455, https://doi.org/10.1016/j.ijbiomac.2020.03.162.

[20] M.E. Abd El-Aziz, A.M. Youssef, S. Kamel, G. Turky, Conducting hydrogel based on chitosan, polypyrrole and magnetite nanoparticles: a broadband dielectric spectroscopy study, Polym. Bull. 76 (2019) 3175–3194, https://doi.org/10.1007/s00289-018-2545-1.

[21] M. Pizzoli, G. Ceccorulli, M. Scandola, Molecular Motions of Chitosan in the Solid State 222, 1991, pp. 205–213, https://doi.org/10.1016/0008-6215(91)89018-B.

[22] A. Nogales, T.A. Ezquerra, D.R. Rueda, F. Martínez, J. Retuert, Influence of water on the dielectric behaviour of chitosan films, Colloid Polym. Sci. 275 (1997) 419–425, https://doi.org/10.1007/s003960050099.

[23] M.T. Viciosa, M. Dionísio, R.M. Silva, R.L. Reis, J.F. Mano, Molecular motions in chitosan studied by dielectric relaxation spectroscopy, Biomacromolecules 5 (2004) 2073–2078, https://doi.org/10.1021/bm049685b.

[24] M.T. Viciosa, Dielectric characterization of neutralized and nonneutralized chitosan upon drying, Biopolymers 81 (2006) 149–159, https://doi.org/10.1002/bip.

[25] J.B. González-Campos, E. Prokhorov, G. Iuna-Bárcenas, A. Fonseca-García, I. C. Sanchez, Dielectric relaxations of chitosan: the effect of water on the α-relaxation and the glass transition temperature, J. Polym. Sci. B Polym. Phys. 47 (2009) 2259–2271, https://doi.org/10.1002/polb.21823.

[26] S. Kumar-Krishnan, E. Prokhorov, M. Ramírez, M.A. Hernandez-Landaverde, D. G. Zarate-Triviño, Y. Kovalenko, I.C. Sanchez, J. Meńdez-Nonell, G. Luna-Bárcenas, Novel gigahertz frequency dielectric relaxations in chitosan films, Soft Matter 10 (2014) 8673–8684, https://doi.org/10.1039/c4sm01804d.

[27] A.M. Salaberría, R. Teruel-Juanes, J.D. Badia, S.C.M. Fernandes, V. Sáenz de Juano-Arbona, J. Labidi, A. Ribes-Greus, Influence of chitin nanocrystals on the dielectric behaviour and conductivity of chitosan-based bionanocomposites, Compos. Sci. Technol. 167 (2018) 323–330, https://doi.org/10.1016/j.compscitech.2018.08.019.
[28] J.B. González-Campos, E. Prokhorov, G. Luna-Bárcenas, I.C. Sanchez, J. Lara-Romero, M.E. Mendoza-Duarte, F. Villaseñor, L. Guevara-Olvera, Chitosan/silver nanoparticles composite: molecular relaxations investigation by dynamic mechanical analysis and impedance spectroscopy, J. Polym. Sci. B Polym. Phys. 48 (2010) 739–748, https://doi.org/10.1002/polb.21941.
[29] E. Strupiechonski, M. Moreno-Ríos, E.O. Ávila-Dávila, R. Román-Doval, E. Prokhorov, Y. Kovalenko, D.G. Zárate-Triviño, D.I. Medina, G. Luna-Barcenas, Relaxation phenomena in chitosan-au nanoparticle thin films, Polymers (Basel) 13 (2021), https://doi.org/10.3390/polym13193214.
[30] N.V. Afanas'Eva, V.A. Petrova, E.N. Vlasova, S.V. Gladchenko, A.R. Khayrullin, B. Z. Volchek, A.M. Bochek, Molecular mobility of chitosan and its interaction with montmorillonite in composite films: dielectric spectroscopy and FTIR studies, Polym. Sci. - Ser. A 55 (2013) 738–748, https://doi.org/10.1134/S0965545X13120018.
[31] J.M. Charlesworth, Deconvolution of overlapping relaxations in dynamic mechanical spectra, J. Mater. Sci. 28 (1993) 399–404, https://doi.org/10.1007/BF00357816.
[32] S. Havriliak, S. Negami, A complex plane representation of dielectric and mechanical relaxation processes in some polymers, Polymer (Guildf) 8 (1967) 161–210, https://doi.org/10.1016/0032-3861(67)90021-3.
[33] S. Havriliak, S. Negami, A complex plane analysis of α-dispersions in some polymer systems, J. Polym. Sci. C Polym. Symp. 14 (1966) 99–117, https://doi.org/10.1002/polc.5070140111.
[34] F. Kremer, A. Schönhals, Broadband Dielectric Spectroscopy, 2003, https://doi.org/10.1007/978-3-642-56120-7.
[35] G.S. Fulcher, Analysis of recent measurements of the viscosity of glasses, J. Am. Ceram. Soc. 75 (1992) 1043–1055, https://doi.org/10.1111/j.1151-2916.1992.tb05536.x.
[36] Q. Qin, G.B. McKenna, Correlation between dynamic fragility and glass transition temperature for different classes of glass forming liquids, J. Non-Cryst. Solids 352 (2006) 2977–2985, https://doi.org/10.1016/j.jnoncrysol.2006.04.014.
[37] K. Kunal, C.G. Robertson, S. Pawlus, S.F. Hahn, A.P. Sokolov, Role of chemical structure in fragility of polymers: a qualitative picture, Macromolecules 41 (2008) 7232–7238, https://doi.org/10.1021/ma801155c.
[38] H.W. Starkweather, Aspects of simple, non-cooperative relaxations, Polymer (Guildf) 32 (1991) 2443–2448, https://doi.org/10.1016/0032-3861(91)90087-Y.
[39] A.K. Jonscher, The "universal" dielectric response, Nature 267 (1977) 673–679, https://doi.org/10.1038/267673a0.
[40] R. Teruel-Juanes, C. del Río, O. Gil-Castell, C. Primaz, A. Ribes-Greus, Triblock SEBS/DVB crosslinked and sulfonated membranes: fuel cell performance and conductivity, J. Appl. Polym. Sci. 138 (2021), https://doi.org/10.1002/app.50671.
[41] X. Qian, N. Gu, Z. Cheng, X. Yang, E. Wang, S. Dong, Methods to study the ionic conductivity of polymeric electrolytes using a.c. impedance spectroscopy, J. Solid State Electrochem. 6 (2001) 8–15, https://doi.org/10.1007/s100080000190.
[42] O. Lopez, M.A. Garcia, M.A. Villar, A. Gentili, M.S. Rodriguez, L. Albertengo, Thermo-compression of biodegradable thermoplastic corn starch films containing chitin and chitosan, Lwt 57 (2014) 106–115, https://doi.org/10.1016/j.lwt.2014.01.024.
[43] C. Palpandi, V. Shanmugam, A. Shanmugam, Extraction of chitin and chitosan from shell and operculum of mangrove gastropod Nerita (Dostia) crepidularia Lamarck, Int. J. Med. Med. Sci. 1 (2009) 198–205.
[44] M.L. Duarte, M.C. Ferreira, M.R. Marvão, J. Rocha, An optimised method to determine the degree of acetylation of chitin and chitosan by FTIR spectroscopy, Int. J. Biol. Macromol. 31 (2002) 1–8, https://doi.org/10.1016/S0141-8130(02)00039-9.
[45] I.F. Amaral, P.L. Granja, M.A. Barbosa, Chemical modification of chitosan by phosphorylation: an XPS, FT-IR and SEM study, J. Biomater. Sci. Polym. Ed. 16 (2005) 1575–1593, https://doi.org/10.1163/156856205774576736.
[46] P. Kolhe, R.M. Kannan, Improvement in ductility of chitosan through blending and copolymerization with PEG: FTIR investigation of molecular interactions, Biomacromolecules 4 (2003) 173–180, https://doi.org/10.1021/bm025689+.
[47] G. Cárdenas, S.P. Miranda, FTIR and TGA studies of chitosan composite films, J. Chil. Chem. Soc. 49 (2004) 291–295, https://doi.org/10.4067/s0717-97072004000400005.
[48] S. Anicuta, L. Dobre, M. Stroescu, I. Jipa, Fourier transform infrared (ftir) spectroscopy for characterization of antimicrobial films containing chitosan, in: Analele Univ. Din Oradea Fasc. Ecotoxicologie, Zooteh. Si Tehnol. Ind. Aliment, 2010, pp. 1234–1240.
[49] I. Corazzari, R. Nisticò, F. Turci, M.G. Faga, F. Franzoso, S. Tabasso, G. Magnacca, Advanced physico-chemical characterization of chitosan by means of TGA coupled on-line with FTIR and GCMS: thermal degradation and water adsorption capacity, Polym. Degrad. Stab. 112 (2015) 1–9, https://doi.org/10.1016/j.polymdegradstab. 2014.12.006.
[50] O. Gil-Castell, R. Teruel-Juanes, F. Arenga, A.M. Salaberria, M.G. Baschetti, J. Labidi, J.D. Badia, A. Ribes-Greus, Crosslinked chitosan/poly(vinyl alcohol)-based polyelectrolytes for proton exchange membranes, React. Funct. Polym. 142 (2019) 213–222, https://doi.org/10.1016/j.reactfunctpolym.2019.06.003.
[51] J. Zawadzki, H. Kaczmarek, Thermal treatment of chitosan in various conditions, Carbohydr. Polym. 80 (2010) 394–400, https://doi.org/10.1016/j.carbpol.2009.11.037.
[52] M.J. Bof, V.C. Bordagaray, D.E. Locaso, M.A. García, Chitosan molecular weight effect on starch-composite film properties, Food Hydrocoll. 51 (2015) 281–294, https://doi.org/10.1016/j.foodhyd.2015.05.018.
[53] I. Leceta, P. Guerrero, I. Ibarburu, M.T. Dueñas, K. De La Caba, Characterization and antimicrobial analysis of chitosan-based films, J. Food Eng. 116 (2013) 889–899, https://doi.org/10.1016/j.jfoodeng.2013.01.022.
[54] R.A. Mauricio-Sánchez, R. Salazar, J.G. Luna-Bárcenas, A. Mendoza-Galván, FTIR spectroscopy studies on the spontaneous neutralization of chitosan acetate films by moisture conditioning, Vib. Spectrosc. 94 (2018) 1–6, https://doi.org/10.1016/j.vibspec.2017.10.005.
[55] C. Branca, G. D'Angelo, C. Crupi, K. Khouzami, S. Rifici, G. Ruello, U. Wanderlingh, Role of the OH and NH vibrational groups in polysaccharide-nanocomposite interactions: a FTIR-ATR study on chitosan and chitosan/clay films, Polymer (Guildf) 99 (2016) 614–622, https://doi.org/10.1016/j.polymer.2016.07.086.
[56] P. Fernandez-Saiz, M.J. Ocio, J.M. Lagaron, Film-forming process and biocide assessment of high-molecular-weight chitosan as determined by combined ATR-FTIR spectroscopy and antimicrobial assays, Biopolymers 83 (2006) 577–583, https://doi.org/10.1002/bip.20589.
[57] J.M. Lagaron, P. Fernandez-Saiz, M.J. Ocio, Using ATR-FTIR spectroscopy to design active antimicrobial food packaging structures based on high molecular weight chitosan polysaccharide, J. Agric. Food Chem. 55 (2007) 2554–2562, https://doi.org/10.1021/jf063110j.
[58] C. Qiao, X. Ma, J. Zhang, J. Yao, Effect of hydration on water state, glass transition dynamics and crystalline structure in chitosan films, Carbohydr. Polym. 206 (2019) 602–608, https://doi.org/10.1016/j.carbpol.2018.11.045.
[59] J. Einfeldt, D. Meißner, A. Kwasniewski, Polymerdynamics of cellulose and other polysaccharides in solid state-secondary dielectric relaxation processes, Prog. Polym. Sci. 26 (2001) 1419–1472, https://doi.org/10.1016/S0079-6700(01)00020-X.
[60] A.A. Ali, M.M. Elmahdy, A. Sarhan, M.I. Abdel Hamid, M.T. Ahmed, Structure and dynamics of polypyrrole/chitosan nanocomposites, Polym. Int. 67 (2018) 1615–1628, https://doi.org/10.1002/pi.5685.
[61] G. Inzelt, Applications of conducting polymers, in: Monographs in Electrochemistry, Berlin, Heidelberg, 2nd ed, 2012, https://doi.org/10.1007/978-3-642-27621-7.
[62] K.A. Mauritz, Dielectric relaxation studies of ion motions in electrolyte-containing perfluorosulfonate ionomers. 4. Long-range ion transport, Macromolecules 22 (1989) 4483–4488, https://doi.org/10.1021/ma00202a018.
[63] H. Bai, H. Zhang, Y. He, J. Liu, B. Zhang, J. Wang, Enhanced proton conduction of chitosan membrane enabled by halloysite nanotubes bearing sulfonate polyelectrolyte brushes, J. Membr. Sci. 454 (2014) 220–232, https://doi.org/10.1016/j.memsci.2013.12.005.
[64] Y. Liu, J. Wang, H. Zhang, C. Ma, J. Liu, S. Cao, X. Zhang, Enhancement of proton conductivity of chitosan membrane enabled by sulfonated graphene oxide under both hydrated and anhydrous conditions, J. Power Sources 269 (2014) 898–911, https://doi.org/10.1016/j.jpowsour.2014.07.075.